

A hemodynamic decomposition model for detecting cognitive load using functional near-infrared spectroscopy

Marco A. Pinto-Orellana^a, Diego C. Nascimento^b, Peyman Mirtaheri^a, Rune Jonassen^c, Anis Yazidi^d, Hugo L. Hammer^e

^a*Department of Mechanical, Electronics and Chemical Engineering, Oslo Metropolitan University.*

^b*Institute of Mathematical Science and Computing, University of São Paulo, São Carlos.*

^c*Department of Health Science, Oslo Metropolitan University.*

^d*Department of Information Technology, Oslo Metropolitan University.*

^e*Department of Information Technology, Oslo Metropolitan University and Simula Metropolitan Center.*

Abstract

In the current paper, we introduce a parametric data-driven model for functional near-infrared spectroscopy that decomposes a signal into a series of independent, rescaled, time-shifted, hemodynamic basis functions. Each decomposed waveform retains relevant biological information about the expected hemodynamic behavior. The model is also presented along with an efficient iterative estimation method to improve the computational speed. Our hemodynamic decomposition model (HDM) extends the canonical model for instances when a) the external stimuli are unknown, or b) when the assumption of a direct relationship between the experimental stimuli and the hemodynamic responses cannot hold. We also argue that the proposed approach can be potentially adopted as a feature transformation method for machine learning purposes. By virtue of applying our devised HDM to a cognitive load classification task on fNIRS signals, we have achieved an accuracy of $86.20\% \pm 2.56\%$ using six channels in the frontal cortex, and $86.34\% \pm 2.81\%$ utilizing only the AFpz channel also located in the frontal area. In comparison, state-of-the-art time-spectral transformations only yield $64.61\% \pm 3.03\%$ and $37.8\% \pm 2.96\%$ under identical experimental settings.

Keywords: Feature engineering; Machine learning; Functional near-infrared spectroscopy.

1. Introduction

Functional near-infrared spectroscopy is a noninvasive neuroimaging technique that measures the hemodynamic response of the brain based on the change of light absorption in the near-infrared spectrum (700nm–900 nm) [1]. Light is emitted on the scalp, and crosses the skull, cerebrospinal fluid, and reaches the cerebral cortex, where the hemodynamic chromophore components scatter and absorb the light according to their optical properties [2]. The primary hemodynamic components in the blood are mainly oxy-hemoglobin (HbO) and deoxy-hemoglobin (HbR) [3]. The modified Beer-Lambert law provides a non-linear relationship that associates fNIRS light intensities with estimates of the local concentration of those components. Based on the neurovascular coupling theory, the information about the oxygenation changes are based on metabolic demands during the brain neural activations [4]. Therefore, fNIRS can be seen as an important brain activity monitoring technique that is complementary to other techniques such as electroencephalography which reflects only the electrical activation of the neurons [5].

Optical spectroscopy, as a brain activity imaging method, is relatively new in the neuroscience community. However, the underlying process measured by the latter technique: either metabolic

or hemodynamic responses of the brain, has been already widely studied through blood-oxygen-level-dependent signal (BOLD) in functional magnetic resonance imaging (fMRI) over the last three decades [6]. Even though fMRI studies are clinically accepted as accurate to identify brain physiological activities, the inherent cost of the equipment, the lack of portability, and the low time resolution, put a restriction on the number and type of experiments that can be performed and analyzed. In contrast, fNIRS provides a reliable alternative to collect hemodynamic data with a time resolution that can be up to ten times higher than their fMRI counterpart, with enhanced portability. However, this comes with the cost of a lower spatial resolution [7].

The research in the field of fNIRS falls into two main families according to their respective focus: clinical and classification oriented studies. Those two research communities aspire to investigate the differences in the signal under the effect of stimuli with their own custom approaches. Clinical studies often focus on quantifying the variations in the recordings when a particular stimulus is applied [2]. On the other hand, classification-oriented studies center their goal on the discovery of nonlinear relationships between stimuli and optical signals in order to devise models to predict the provoking stimulus from a new set of signals, with a certain degree of accuracy [8].

In clinical settings, fNIRS studies rely on the comparison of time-domain properties of the signals. It is assumed that the underlying biological process is a linear time-invariant stimulus-guided process with a noise component, which is modeled as a Gaussian random variable [3]. Hence, the signal amplitude difference between a phenomenon of interest and a control case along with its statistical significance can be assessed through the estimation of the first and second statistical noncentral moments. The uncertainty of this difference is usually expressed through confidence intervals or p-values [4, 5, 9].

Clinical procedures are shown to be accurate in revealing specific spatial-temporal patterns in brain activity. It was determined that particular regions of the brain are more "activated" than others under specific circumstances or stimuli. It should be perceived that, in this context, "activation" denotes a high instantaneous amplitude with respect to the baseline observed mean.

A common method in experimental BOLD-fMRI studies is modeling the fMRI signal with a generalized linear model (GLM) where the design matrix - i.e., the set of regressors of interest - is constructed with a sequence of canonical hemodynamic response functions (HRFs) [10]. HRFs are significant models of time-domain brain metabolic activity, providing a series of measures with psycho-physiological interest: amplitude, delay, and duration of the hemodynamic process [11]. GLM-HRF in fNIRS data is known to be reliable for detecting differences in the activation patterns in the visual cortex [12, 6].

For classification-oriented tasks, machine learning methods exhibit high performance in activity prediction due to their ability to explore and discover nonlinear structures in the data. In contrast with other classification fields, recent studies have been inconclusive in determining a predominant algorithm that can outperform all classification tasks when fNIRS is involved. Levels of pain can be detected with support vector machines with 94% accuracy [13]. Differentiation between word generation, motor imagery, and mental arithmetic yielded an accuracy as low as 66% with a deep neural network [7] while discrimination between visual and auditory stimuli reached an accuracy of 97.8% with support vector machine (and additional features extracted from EEG) [14]. In contrast to the nonlinear models, the accomplished accuracy in emotion classification was 71.9% using linear discriminant analysis (LDA) [8]. Moreover, speech activity identification obtained an accuracy of 74.7% using generalized canonical correlation analysis [15]. This diversity of algorithms with a large variability of accuracy coincides with the no free lunch theorem that states that "*no algorithm can be good for any arbitrary prior*" information [16].

Despite the effectiveness of machine learning methods in classification oriented studies, the complexity associated with the interpretability of the nonlinear models, generally more flexible, although

limits their use in clinical studies [13]. In the latter, the explanation of underlying physiological processes is more valuable [17]. Mathematical models with enough complexity to provide high predictive performance, but based on interpretable and physiological-supported models, then this gap shall be solved.

In this paper, we propose a parametric method: the hemodynamic decomposition model (HDM), which aims to satisfy the requirements of both types of fNIRS analysis. HDM explains a metabolic signal, such as oxy- or deoxy-hemoglobin, as a sum of a series of independent bases. Each basis function is a simplified version of the canonical hemodynamic response function for sensorimotor activities while keeping a clear theoretical description of the underlying metabolic activity. HDM also provides enough information as a feature input for prediction-oriented purposes showing an exceptional predictive power in machine learning algorithms under different circumstances.

The remainder of this paper is organized into three additional sections: the description of the model and the iterative estimation method (section 2); the analysis of the potential of HDM for machine learning tasks using real fNIRS data (section 3); and our conclusions (section 4.)

2. Model

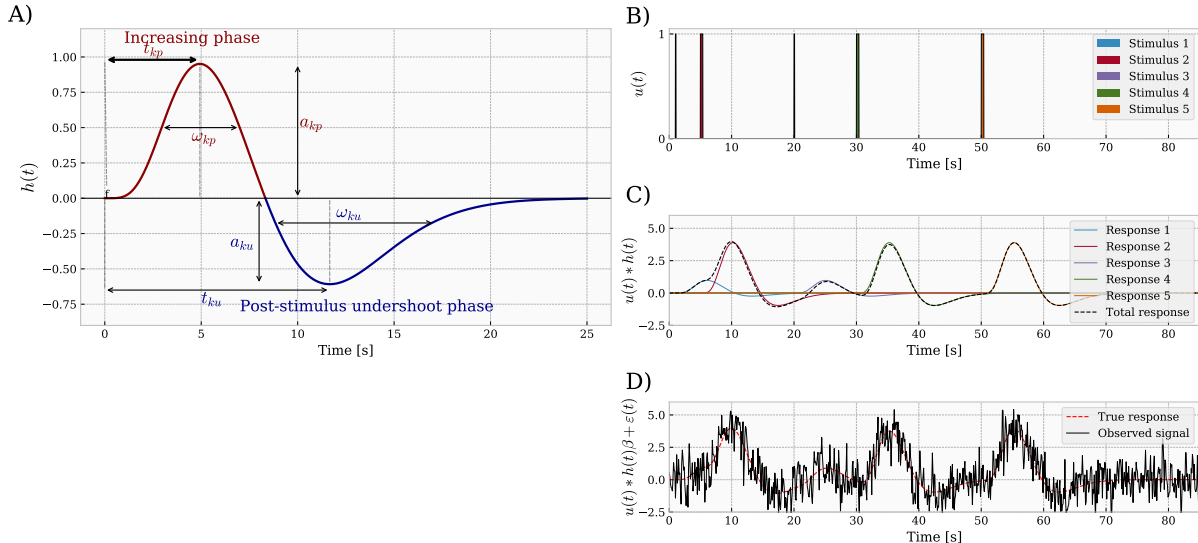


Figure 1: Subject-level GLM of a hemodynamic data with the canonical HRF. (A) Components of the canonical double-gamma HRF, considering the GLM. (B) Hypothetical triggered set of stimuli $u(t)$. (C) Hemodynamics modelling, estimating the causes a change, with a convolution operation $u(t) * h(t)$. (D) Empirical distorted and noised signal $u(t) * h(t) + \epsilon(t)$. These four panels represent the canonical HRF decomposition for sensorimotor activities.

Hemodynamic signals, within-subjects, are modeled as linear time-invariant systems using theoretical hemodynamic response functions (HRFs) as a foundation. An HRF is a function that represents the typical oscillation phases in the blood dynamics. The de facto model for hemodynamic data, originally defined for fMRI time series, defines the output signal $y(t)$ as the convolution of a stimulus function $u(t)$ and an HRF $h(t)$ with an additive noise component [18, 19]:

$$y(t) = x(t) \beta + \epsilon(t) \quad (1)$$

$$x(t) = u(t) * h(t) \quad (2)$$

where $*$ is the convolution operator, β is the regression parameter, while $\varepsilon(t)$ models the noise. Subsequent measurements in BOLD-fMRI signals show correlated noise. Therefore, this behavior is modeled through a first-order autoregressive noise [20]:

$$\varepsilon(t) = \rho\varepsilon(t-1) + \eta(t) \quad (3)$$

where $\eta(t)$ is a Gaussian white noise $\eta(t) \sim \mathcal{N}(0, \sigma^2)$ with a variance σ^2 . A simulation of the hemodynamic representation performed by this model is depicted in Figure 1b-d.

It is worth mentioning that there is not a unique and general HRF, and in order to guarantee that the GLM's parameters could be estimated from the data, there are three conditions that a HRF must meet: a) to start and end at zero; b) to be smooth, or at least, have continuity in the first and second derivatives [17]; and c) to be a causal function, i.e., it should only depend on current or previous values [21].

Several types of basis HRFs that fulfill the aforementioned conditions have been proposed which include: Fourier sets, finite impulse response functions, and gamma-based functions [22] to mention a few. Among the alternatives, the single- and double-gamma HRFs are the most common in the literature and also integrated in the standard toolboxes [18]. The two-gamma HRF, also known as the canonical hemodynamic response function, described in [22], models the increasing and decreasing (or undershoot) phases of the metabolic process with two gamma functions:

$$h(t) = g(t; a_i, \omega_i, t_i) - g(t; a_d, \omega_d, \tau_d) \quad (4)$$

$$g(t; a, \omega, \tau) = a \left(\frac{t}{\tau}\right)^\kappa \exp\left(-\kappa \frac{t-\tau}{t}\right) \quad (5)$$

$$\kappa = (8 \ln 2) \left(\frac{\tau}{\omega}\right)^2 \quad (6)$$

where $g(\cdot)$ is the gamma function characterized by three parameters: response height a , time-to-peak τ , and dispersion or full-width at half-maximum ω as defined in [23, 24]. $g(a_i, \omega_i, t_i)$ and $g(a_d, \omega_d, t_d)$ model the increasing and decreasing, or undershoot, phases of a typical hemodynamics.

A visual description of the six parameters (three per gamma function) of the canonical HRF with the standard values for sensorimotor activities ($a_i = 1$, $\omega_i = 5.2$, $\tau_i = 5.4$, $a_d = 0.35$, $\omega_d = 10.8$, $\tau_d = 7.35$ [24]) is shown in Figure 1a. It should be denoted that these reference values are not universally accepted; some authors argue that the canonical HRF should be a double-gamma with its peak delay at, approximately, six seconds, undershoot delay of sixteen seconds, and with a peak-undershoot amplitude ratio of six [23]. However, in this paper we rely on those parameter values as in [22] and [24].

From the abovementioned model, two fundamental properties should be emphasized: a) the convolution $u(t) * h(t)$ produces, under certain conditions, a curve that is approximately another gamma-function with a dispersion proportional to the stimulus duration [23, 25], and b) the canonical HRF can be considered as an extension of a single gamma function model with a negative single gamma function explaining the undershoot phase. When there is no apparent undershoot in the observations, the single gamma model can also provide a good fit [26, 24]. Thus, it is reasonable to conceive that the combination of GLM and HRF (GLM+HRF) can be reformulated as a concatenation of individual successive gamma functions with duration proportional to the span of each impulse, and with positive or negative amplitudes.

Relying on the same principles, we propose a hemodynamic decomposition model (HDM) where the observed hemodynamic signals (sampled every T_h seconds) are represented as a sequence of a

finite and unknown K number of triggered responses $h_k(t)$:

$$y(t) = \sum_{k=1}^K h_k(t) + \varepsilon(t) \quad (7)$$

$$h_k(t) = a_k g_0 \left(\frac{t - \tau_k + \tau_0}{\omega_k / \omega_0} \right) \quad (8)$$

where $y(t)$ is the autocorrelation effect, $h_k(t)$ is the triggered responses, $\varepsilon(t)$ is the random fluctuations, and $g_0(t)$ is a the positive gamma cycle of a sensorimotor standard HRF, for instance, $g_0(t) = g(t; a_0 = 1, \omega_0 = 5.2, \tau_0 = 5.4)$. Furthermore, the random fluctuations (noise) are Gaussian-distributed ($\varepsilon(t) \sim \mathcal{N}(0, \sigma_\varepsilon^2)$): $\varepsilon(t) = \theta_\varepsilon y(t - T_h) + \epsilon(t)$.

HDM models the measured signal as a sum of shifted, expanded, and scaled kernel waves. Semantically, this representation is not in conflict with the foundational claims of the GLM+HRF model. But, HDM enables representing those circumstances when the stimuli do not generate any noticeable reaction or when the response appears before or after the stimulus.

In order to describe the model in a formal framework, let us define a set $\Omega = \{(a_k, \omega_k, \tau_k)\}_{k=1}^K$ that represents the three main parameters of an HRF: amplitude, duration, and starting time, respectively. The conditional log-likelihood of $N+1$ sampled points from $y(N T_h), y(T_h), \dots, y((N-1) T_h)$ θ_ε , (Equation (7)) and with respect to a known initial point y_0 and σ_ε^2 is given as follows

$$\begin{aligned} \log \mathcal{L}(\Omega, \theta_\varepsilon, \sigma_\varepsilon^2) &= \\ &= \log f_{\Omega, \theta_\varepsilon, \sigma_\varepsilon^2, y(0)=y_0}(y((N-1) T_h), \dots, y(0 \cdot T_h)) \\ &= -\frac{N}{2} \log(2\pi) - \frac{N}{2} \log \sigma_\varepsilon^2 - \frac{1}{2\sigma_\varepsilon^2} \sum_{n=1}^N (S_n^*)^2, \end{aligned} \quad (9)$$

$$S_n^* = \delta_n - \theta_\varepsilon y((n-1) T_h) \quad (10)$$

$$\delta_n = y(n T_h) - \sum_{k=1}^K h_k(n T_h) \quad (11)$$

The conditional maximum likelihood estimator $(\Omega, \theta_\varepsilon, \sigma_\varepsilon^2)$ can be obtained by minimizing $\log \mathcal{L}(\Omega, \theta_\varepsilon, \sigma_\varepsilon^2)$. Details about the numerical optimization for this estimator is given in the next subsection.

2.1. Numerical optimization algorithm

By analogy to a mixture model with an L_2 distance, the MLE estimators of the model described in Equation 9 can have several local optima, and therefore, gradient descent methods are not the most effective numerical techniques to estimate the parameters. First, we expect that a low pass filter will already remove the high-frequency noise during the preprocessing of fNIRS. Therefore, we focus on modeling the low-frequency random fluctuations ($\theta_\varepsilon > 0$.) Hence,

$$\hat{\Omega} = \arg \min_{\Omega} \sum_{n=1}^N (S_n^*)^2 = \arg \min_{\Omega} \sum_{n=1}^N (\delta_n)^2 \quad (12)$$

where S_n^* and δ_n are defined as in Equation 10 and Equation 11.

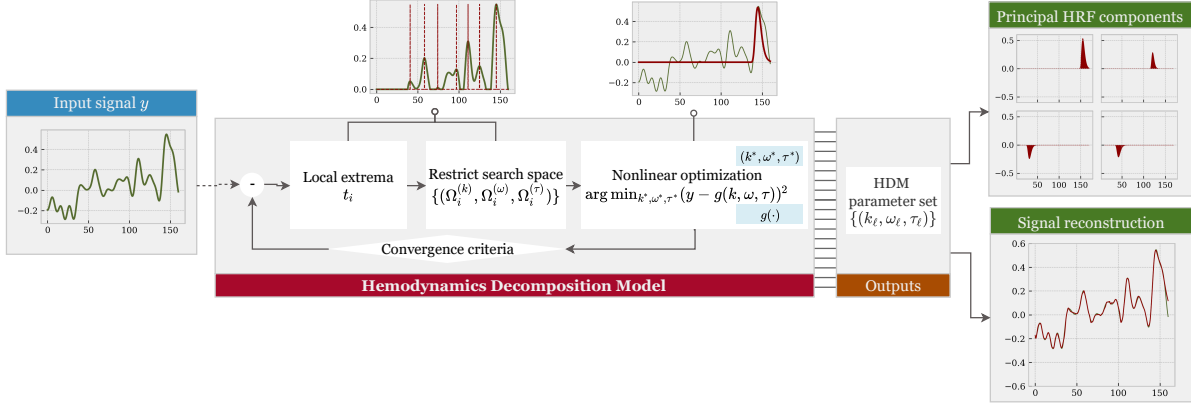


Figure 2: Hemodynamic chartflow decomposition process. The input signal is observed (left-hand panel), and the HDM initialized (decomposing the local extrema and restrict search space, centered-top panels) then a nonlinear optimization is conducted seeking the convergence criteria, resulting in signal partitions (right-hand panels).

Second, due to the high computational complexity, we consider $\hat{\Omega}$ to be an accurate approximation whenever the squared Euclidean distance (or squared L_2 norm), between the modeled HRFs and the observed discrete signal is less than a radius of convergence ξ :

$$\sum_{n=1}^N (\delta_n)^2 \leq \xi \quad (13)$$

Third, to ensure a consistent parameter estimation, we introduce an iterative estimation approach (Figure 2) for constructing the parameter search space:

- Construct $\{(t_i, y_i)\}$ as a set of M local extreme points, i.e., those points such where $\left. \frac{dy}{dt} \right|_{t=t_i} = 0$.
- For each time index t_i , define three sets: $\Omega_a = [\kappa_{a0}y_i, y_i]$, $\Omega_\omega = [\omega_\epsilon, \omega_m]$, $\Omega_\tau = [\kappa_{\tau0}\tau_0, \kappa_{\tau1}\tau_0]$. Ω_τ describes the potential ranges where the hemodynamic impulse are expected to be produced. According to [23] and [24], the common starting time is located from five to sixteen seconds before an observed peak ($\kappa_{\tau0} = 0.8$, $\kappa_{\tau0} = 3$). Ω_ω outlines the feasible choices for the duration. Based on [23] and [22], the maximum observed duration experimentally is slightly higher than seven seconds in sensorimotor stimuli; therefore, we set $\omega_m = 8$. The lowerbound ω_ϵ was empirically set to 0.1 seconds in our experiments. Finally, Ω_a denotes the search space of HRF amplitudes. We prioritize those components that explain most of the observed amplitudes. Consequently, we define the upperbound as the observed amplitude y_i , and the lower limit as a proportion of y_i . Furthermore, in our analysis we set $\kappa_{a0} = 0.8$.
- For each triplet $(\Omega_a, \Omega_\omega, \Omega_\tau)$ related to the time t_i , we use the Broyden–Fletcher–Goldfarb–Shanno optimization algorithm to optimize the best parameters (a^*, ω^*, τ^*) that minimize the L_2 distance between the estimation and the observations in the time interval $[t_i, t_i + 2 \max(\Omega_\tau)]$. Due to the waveform of the gamma-function, we submit that the component effect outside the interval will not be significant. The previous constraints not only guarantee finding the best component that locally explains the input signal, but also reduce the computational time due to a supplementary contraction in the search space.
- Define $R^{(0)} = y(t)$, and let $R^{(\ell)}$ and $r^{(\ell)}$ be residuals of the ℓ -th iteration: $R^{(\ell)} = R^{(\ell-1)} - a^* g_0 \left(\frac{t-a^*+\tau_0}{a^*/\omega_0} \right)$ and $r^{(\ell)}$ the residual sum of squares $r^{(\ell)} = |R^{(\ell)}|^2$. The previous steps can be repeated until $r^{(\ell)}$ reaches the threshold error ξ or L iterations.

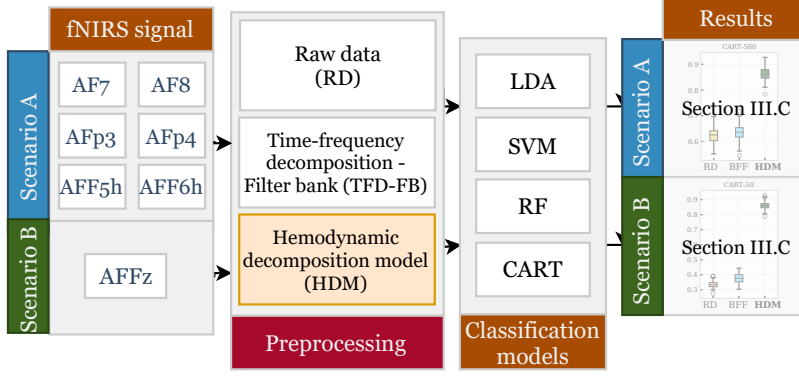


Figure 3: Visual summary of the experimental framework.

- Given the set of estimators $\{(a_i^*, \omega_i^*, \tau_i^*)\}_i$, the autocorrelation parameter $\hat{\theta}_\varepsilon$ is obtained using least square estimation:

$$\hat{\theta}_\varepsilon = \arg \min_{\theta_\varepsilon} \sum_{n=1}^N (\delta_n^* - \theta_\varepsilon y((n-1)T_h))^2 \quad (14)$$

$$\delta_n^* = y(nT_h) - \sum_{k=1}^K a_k^* g_0 \left(\frac{nT_h - \tau_k^* + \tau_0}{\omega_k^* / \omega_0} \right) \quad (15)$$

3. Experimental analysis

In this section, we explore the potential of our proposed decomposition technique –HDM–, in the role of the methodological framework combined with the feature extraction method in a machine learning context as it is illustrated in Figure 3. We define a classification problem with the goal of predicting the cognitive level related to an activity that a subject is performing based on his hemodynamic signals.

3.1. Dataset

The dataset of the experiment comprises oxy- and deoxy-hemoglobin signals estimated from the fNIRS using the modified Beer-Lambert law. For repeatability purposes, a publicly available dataset is being used for our pilot analysis which comes from a series of experiments performed by Shin et al. at the Technische Universität Berlin involving "n-back" tasks [27]. Their study was restricted to 29 subjects in the age group of 20-30 years old. We rather focused on one of their experiments: n-back tasks, which are accurate markers of brain workload [28]. The dataset contains a series of sessions, where each session protocol is composed of four steps: a) show a straightforward instruction for 2 seconds; b) request the subject to perform the task (0-, 2-, and 3-back); c) ring a short beep for 250ms; and d) rest for 20 seconds. For further information about the experimental protocol, we refer the reader to [27]. The fNIRS signals in the dataset were sampled at 10Hz on 36 channels. For the purpose of this study, we selected seven channels in the frontal cortex: AF7, AF8, AFF5h, AFF6h, AFp3, AFp4, and AFpz, according to the EEG 10-20 standard layout position, as it is shown in Figure 4 [27].

3.2. Experimental setting

Based on the complete dataset provided by Shin et al. [27], we configured two simulation scenarios to test our method:

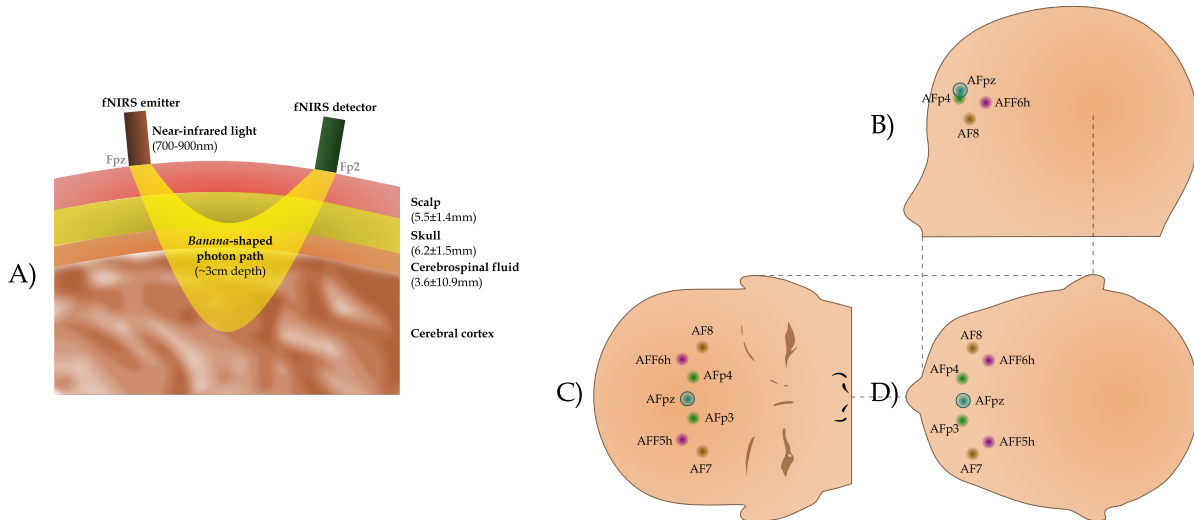


Figure 4: Principles and measurement settings of fNIRS. (A) Illustration of the the working principle of fNIRS, that is, a Physiological channels used in the analysis. The selected seven fNIRS channels, placed in the frontal cortex, are showed in panels (B) side, (C) front, and (D) top view.

- Scenario A: classification using six channels from the frontal region: AF7, AF8, AFF5, AFF6, AFp3, AFp4 (Figure 4) with data from the “subject 01.” This setting will expose the ability of the hemodynamic decomposition method to provide relevant information in machine learning algorithms as it is known that cognitive load manifests with activations in the frontal cortex [29].
- Scenario B: workload identification using only the channel AFpz (frontal region slightly over the root of the nose, Figure 4). In contrast with the previous simulation, due to the reduced amount of data used in this setting, this scenario is assessed with data from subjects 01-26. The results of this simulation will assess the capabilities of our method under spatially limited data.

To compare the efficiency of our model as a pre-processing technique, we establish two alternative feature sets: raw time-domain signals, and time-frequency features. The time-frequency decomposition (TFD) is based on a filter bank structure (FB): we define five 100th-order finite-impulse-response band-pass filters in the ranges: 0-0.02Hz, 0.02-0.04Hz, 0.06-0.08Hz, and 0.08-0.10Hz. These intervals are known to contain the most relevant information related to hemodynamic processes, and Appriou et al. showed that the TFD-FB provides a prediction accuracy of $67.9\% \pm 8.1\%$ [30].

For each feature extraction technique, we applied four basic machine algorithms and compare their performance: support vector machines (SVM) [13, 14], random forests (RF) [31, 32] classification and regression trees (CART) [33], and linear discriminant analysis (LDA) [30]. These algorithms were selected, given their proven efficiency to solve other classification tasks were fNIRS was involved. Based on the literature results [30], there were no significant differences between the performance of recursive neural networks respect with LDA with features extracted with filter banks. Due to this reason and the lack of longer time series per subject, deep learning routines were not included in this comparison. For further details about the applied algorithms, we refer to [13, 32, 33, 30].

Physiological signals hold substantial information about their time dependency structure. In order to keep this structure in our experimental setting, the validation method consisted of a sliding window train-test (SWTT) [34]: the algorithm predicted the following activities in 2 seconds using

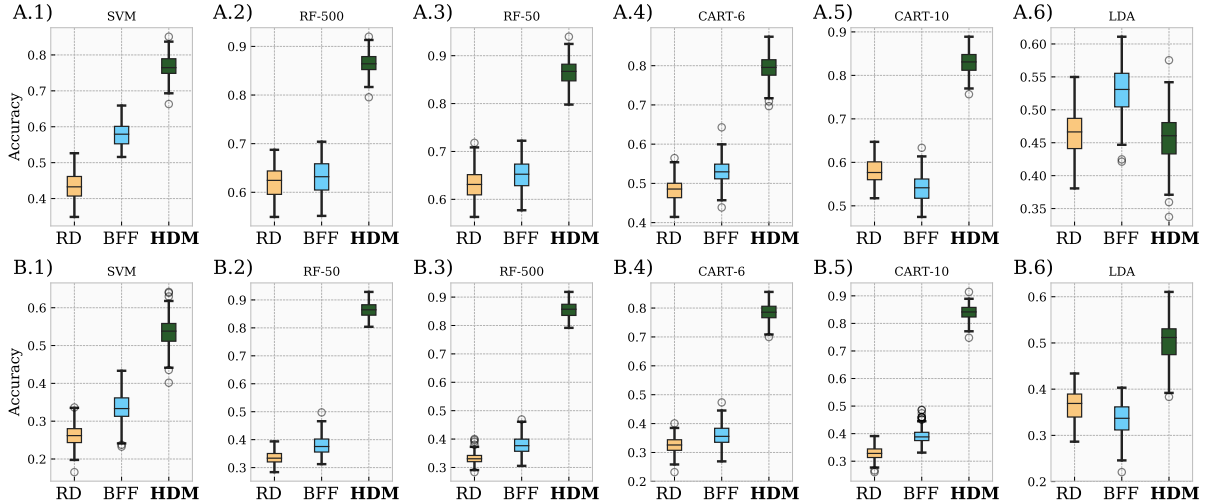


Figure 5: Performance of HDM in activity recognition on the two different brain region, adopting six machine-learning algorithms, based on three data pre-processing. Scenario A (top panels): data gathered from the six frontal-cortex channels: AF7, AF8, AFF5, AFF6, AFp3, and AFp4 of subject 01. Scenario B (bottom panels): data collected from subject 01 from only channel AFpz.

Six machine-learning algorithms were compared (each panel from the left to the right): 1) SVM; 2) random forest with 50 trees and 3) 500 trees; 4) decision trees (CART) with 6 depth levels and 5) 10 levels; and 6) LDA classifier. The abscissa axis represents the type of input on the algorithms: raw data (RD), bank filter features (BFF), and HDM. In all evaluations, box plots show the second and third quantile of the results using SWTT. Empirical results showed the outperformance of the HDM across almost all classifiers.

the information from the previous 60 seconds. This estimation technique is known for being unbiased with a moderately low variance [35].

3.3. Results

Since the distribution of the four labels (0-back, 2-back, 3-back, and rest) is balanced across the dataset, the accuracy is a proper metric of the algorithms’ performance, and thus it is used to compare the outcomes. We compiled the results of the experimental scenario A (with frontal cortex data) and B (with single-channel signals) from “subject 01” in Figure 5.

From the empirical results, there are a few noteworthy observations regarding the performance of the different machine learning algorithms:

- Random forests showed more success at identifying cognitive load states regardless of the experimental setting. These results are also concordant with the conclusions found in previous studies [30].
- Support vector machines (SVM) did not exhibit the best performance in our experiments. We examine this behavior using the cumulative confusion matrices of Table B.2 and B.3. Even though SVM performs worse than the other algorithms, it can recognize the n-back activities, but it exhibits a high level of uncertainty when differentiating those states from their respective rest periods. However, the level of uncertainty among n-back activities is minimal when using HDM with respect to TFD-FB or raw data.
- By comparing experiments A and B, it is evident that the performance drops when the input data is restricted to one channel. The only two exceptions are linear discriminant analysis and random forests with the decomposition model HDM. The sensibility of LDA improves by

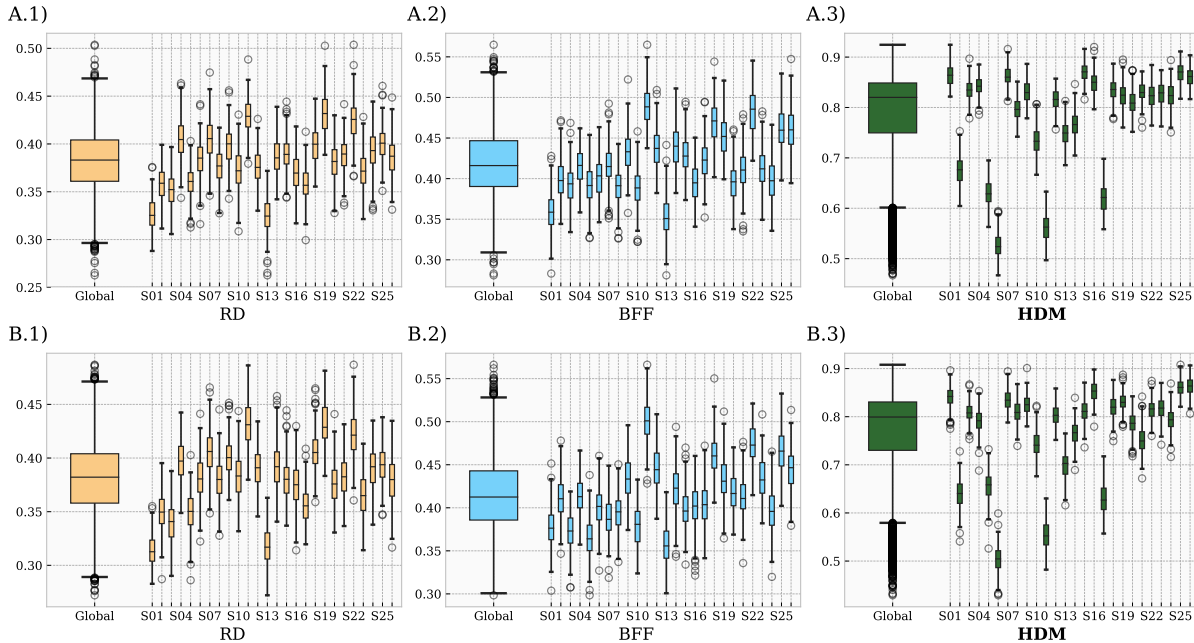


Figure 6: Subject-level performance of HDM in a single-channel activity-recognition in 26 subjects. Three preprocessing methods were compared: 1) raw data (RD), left-hand panels, and bank filter features (BFF), center panels, and 3) HDM, right-hand panels. Two algorithms were applied: A) random forest with 50 trees (top panels); B) Decision trees CART –10-level depth– (bottom panels). The identifier of the subject from whom data is collected is shown in the x-axis for each plot. Note that HDM provides a higher accuracy with both classification models.

8.88% and its precision by 11.1%. Random forests maintain identical performance across both cases.

- Decision trees do not exhibit a substantial difference with the SVM alternatives where TFD-FB and raw data are the input features. Nevertheless, they yield attractive accuracy metrics when HDM is utilized: between 73.2% and 83.8%. HDM produces a non-linearly mapping of each task into hemodynamic responses, and we hypothesize that decision trees are partially detecting those non-linear boundaries.

The results indicate that the increment of the prediction power using HDM is not intrinsically associated with one specific family of ML algorithms. We can argue that HDM is a proper method to extract relevant features from the fNIRS signals. However, the precision of brain activity detection will rely on the chosen algorithm. Additionally, the remarkable results of the decision trees in experiment B are promissory for further development of fNIRS activity recognition systems, especially implemented in devices with hardware restrictions or real-time architectures (due to the low time complexity of training CART methods).

4. Conclusion

We propose an appealing representation of fNIRS signals using a hemodynamic decomposition model (HDM) that has an intuitive physiological interpretation. It models the observed signal as a sum of independent hemodynamic responses, where each one is based on the canonical HRF, but rescaled in duration and amplitude, and triggered at different instants. Estimating those parameters

and the number of HRFs that accurately model the hemodynamic signals is time-exhaustive, non-convex optimization problem. To cope with this problem, we present an iterative estimation process that maximizes the accuracy of the signal and allows us to control the precision of the representation using only two hyper-parameters: the number of maximum iterations and the convergence ratio.

Due to the data-driven nature of the HDM model, no additional information about the stimuli in the experiment is required. Nevertheless, the method can be combined with registered stimuli as a feature extraction method for machine learning algorithms in prediction/classification tasks. We investigated the case of brain cognition load prediction under a classical experiment setting (n-back). Raw data and time-frequency features were compared with our decomposition model using different classification methods including support vector machines, decision trees and random forests. We conclude that our method has a clear advantage as a feature transformation regardless of the deployed algorithm. HDM yields an improvement in the accuracy by up to 21.59% and 23.69% with respect to time-spectral and raw data features, respectively.

5. Funding

This work is financially supported by the Research Council of Norway to the Project No. 273599, "Patient-Centric Engineering in Rehabilitation (PACER)". Diego C. Nascimento is partially supported by the Brazilian funding agency "Coordenação de Aperfeiçoamento de Pessoal de Nível Superior" (CAPES).

References

- [1] H. Y. Kim, K. Seo, H. J. Jeon, U. Lee, and H. Lee, "Application of functional near-infrared spectroscopy to the study of brain function in humans and animal models," *Molecules and cells*, vol. 40, no. 8, p. 523, 2017.
- [2] F. Herold, P. Wiegel, F. Scholkmann, and N. G. Mueller, "Applications of functional near-infrared spectroscopy (fnirs) neuroimaging in exercise-cognition science: a systematic, methodology-focused review," *Journal of clinical medicine*, vol. 7, no. 12, p. 466, 2018.
- [3] S. Tak and J. C. Ye, "Statistical analysis of fNIRS data: A comprehensive review," *NeuroImage*, vol. 85, pp. 72–91, jan 2014. [Online]. Available: <https://doi.org/10.1016/j.neuroimage.2013.06.016>
- [4] M. J. Herrmann, A. K. Horst, S. Loble, M. T. Mill, A. Katzorke, and T. Polak, "Relevance of dorsolateral and frontotemporal cortex on the phonemic verbal fluency – a fNIRS-study," *Neuroscience*, vol. 367, pp. 169–177, dec 2017. [Online]. Available: <https://doi.org/10.1016/j.neuroscience.2017.10.028>
- [5] G. Pellegrino, A. Machado, N. von Ellenrieder, S. Watanabe, J. A. Hall, J.-M. Lina, E. Kobayashi, and C. Grova, "Hemodynamic response to interictal epileptiform discharges addressed by personalized EEG-fNIRS recordings," *Frontiers in Neuroscience*, vol. 10, mar 2016. [Online]. Available: <https://doi.org/10.3389/fnins.2016.00102>
- [6] M. A. Yucel, J. Selb, C. M. Aasted, P.-Y. Lin, D. Borsook, L. Becerra, and D. A. Boas, "Mayer waves reduce the accuracy of estimated hemodynamic response functions in functional near-infrared spectroscopy," *Biomedical Optics Express*, vol. 7, no. 8, p. 3078, jul 2016. [Online]. Available: <https://doi.org/10.1364/boe.7.003078>

- [7] J. Hennrich, C. Herff, D. Heger, and T. Schultz, “Investigating deep learning for fNIRS based BCI,” in *2015 37th Annual International Conference of the IEEE Engineering in Medicine and Biology Society (EMBC)*. IEEE, aug 2015. [Online]. Available: <https://doi.org/10.1109/embc.2015.7318984>
- [8] S. Moghimi, A. Kushki, S. Power, A. M. Guerguerian, and T. Chau, “Automatic detection of a prefrontal cortical response to emotionally rated music using multi-channel near-infrared spectroscopy,” *Journal of Neural Engineering*, vol. 9, no. 2, p. 026022, mar 2012. [Online]. Available: <https://doi.org/10.1088/1741-2560/9/2/026022>
- [9] I. M. Wiggins, C. A. Anderson, P. T. Kitterick, and D. E. Hartley, “Speech-evoked activation in adult temporal cortex measured using functional near-infrared spectroscopy (fNIRS): Are the measurements reliable?” *Hearing Research*, vol. 339, pp. 142–154, sep 2016. [Online]. Available: <https://doi.org/10.1016/j.heares.2016.07.007>
- [10] J. A. Mumford, J.-B. Poline, and R. A. Poldrack, “Orthogonalization of regressors in fMRI models,” *PLOS ONE*, vol. 10, no. 4, p. e0126255, apr 2015. [Online]. Available: <https://doi.org/10.1371/journal.pone.0126255>
- [11] D. A. Handwerker, J. M. Ollinger, and M. D’Esposito, “Variation of BOLD hemodynamic responses across subjects and brain regions and their effects on statistical analyses,” *NeuroImage*, vol. 21, no. 4, pp. 1639–1651, apr 2004. [Online]. Available: <https://doi.org/10.1016/j.neuroimage.2003.11.029>
- [12] T. J. Huppert, “Commentary on the statistical properties of noise and its implication on general linear models in functional near-infrared spectroscopy,” *Neurophotonics*, vol. 3, no. 1, p. 010401, mar 2016. [Online]. Available: <https://doi.org/10.1117/1.nph.3.1.010401>
- [13] R. F. Rojas, X. Huang, and K.-L. Ou, “A machine learning approach for the identification of a biomarker of human pain using fNIRS,” *Scientific Reports*, vol. 9, no. 1, apr 2019. [Online]. Available: <https://doi.org/10.1038/s41598-019-42098-w>
- [14] F. Putze, S. Hesslinger, C.-Y. Tse, Y. Huang, C. Herff, C. Guan, and T. Schultz, “Hybrid fNIRS-EEG based classification of auditory and visual perception processes,” *Frontiers in Neuroscience*, vol. 8, nov 2014. [Online]. Available: <https://doi.org/10.3389/fnins.2014.00373>
- [15] Y. Liu and H. Ayaz, “Speech recognition via fNIRS based brain signals,” *Frontiers in Neuroscience*, vol. 12, oct 2018. [Online]. Available: <https://doi.org/10.3389/fnins.2018.00695>
- [16] S. P. Adam, S.-A. N. Alexandropoulos, P. M. Pardalos, and M. N. Vrahatis, “No free lunch theorem: A review,” in *Approximation and Optimization*. Springer International Publishing, 2019, pp. 57–82. [Online]. Available: https://doi.org/10.1007/978-3-030-12767-1_5
- [17] G. Marrelec, P. Ciuciu, M. Pelegrini-Issac, and H. Benali, “Estimation of the hemodynamic response in event-related functional MRI: Bayesian networks as a framework for efficient bayesian modeling and inference,” *IEEE Transactions on Medical Imaging*, vol. 23, no. 8, pp. 959–967, aug 2004. [Online]. Available: <https://doi.org/10.1109/tmi.2004.831221>
- [18] F. Cignetti, E. Salvia, J.-L. Anton, M.-H. Grosbras, and C. Assaiante, “Pros and cons of using the informed basis set to account for hemodynamic response variability with developmental data,” *Frontiers in Neuroscience*, vol. 10, jul 2016. [Online]. Available: <https://doi.org/10.3389/fnins.2016.00322>

- [19] K. Friston, P. Fletcher, O. Josephs, A. Holmes, M. Rugg, and R. Turner, “Event-related fMRI: Characterizing differential responses,” *NeuroImage*, vol. 7, no. 1, pp. 30–40, jan 1998. [Online]. Available: <https://doi.org/10.1006/nimg.1997.0306>
- [20] A.-K. Seghouane and A. Shah, “Consistent estimation of the fMRI hemodynamic response function in AR(1) noise,” in *2015 IEEE 12th International Symposium on Biomedical Imaging (ISBI)*. IEEE, apr 2015. [Online]. Available: <https://doi.org/10.1109/isbi.2015.7163829>
- [21] S. Makni, P. Ciuciu, J. Idier, and J. Poline, “Joint detection-estimation of brain activity in fMRI using an autoregressive noise model,” in *3rd IEEE International Symposium on Biomedical Imaging: Macro to Nano, 2006*. IEEE, 2006. [Online]. Available: <https://doi.org/10.1109/isbi.2006.1625101>
- [22] G. H. Glover, “Deconvolution of impulse response in event-related BOLD fMRI1,” *NeuroImage*, vol. 9, no. 4, pp. 416–429, apr 1999. [Online]. Available: <https://doi.org/10.1006/nimg.1998.0419>
- [23] W. Penny, K. Friston, J. Ashburner, S. Kiebel, and T. Nichols, *Statistical Parametric Mapping: The Analysis of Functional Brain Images*. Elsevier Science, 2011. [Online]. Available: https://books.google.no/books?id=G_qdEsDlkp0C
- [24] W. Yan, D. Rangaprakash, and G. Deshpande, “Aberrant hemodynamic responses in autism: Implications for resting state fMRI functional connectivity studies,” *NeuroImage: Clinical*, vol. 19, pp. 320–330, 2018. [Online]. Available: <https://doi.org/10.1016/j.nicl.2018.04.013>
- [25] U. Blahak, “Efficient approximation of the incomplete gamma function for use in cloud model applications,” *Geoscientific Model Development*, vol. 3, no. 2, pp. 329–336, jul 2010. [Online]. Available: <https://doi.org/10.5194/gmd-3-329-2010>
- [26] G. M. Boynton, S. A. Engel, G. H. Glover, and D. J. Heeger, “Linear systems analysis of functional magnetic resonance imaging in human v1,” *The Journal of Neuroscience*, vol. 16, no. 13, pp. 4207–4221, jul 1996. [Online]. Available: <https://doi.org/10.1523/jneurosci.16-13-04207.1996>
- [27] J. Shin, A. von Luhmann, D.-W. Kim, J. Mehnert, H.-J. Hwang, and K.-R. Muller, “Simultaneous acquisition of EEG and NIRS during cognitive tasks for an open access dataset,” *Scientific Data*, vol. 5, no. 1, feb 2018. [Online]. Available: <https://doi.org/10.1038/sdata.2018.3>
- [28] A. C. Whiteman, H. Santosa, D. F. Chen, S. Perlman, and T. Huppert, “Investigation of the sensitivity of functional near-infrared spectroscopy brain imaging to anatomical variations in 5- to 11-year-old children,” *Neurophotonics*, vol. 5, no. 01, p. 1, sep 2017. [Online]. Available: <https://doi.org/10.1117/1.nph.5.1.011009>
- [29] F. S. Racz, P. Mukli, Z. Nagy, and A. Eke, “Increased prefrontal cortex connectivity during cognitive challenge assessed by fnirs imaging,” *Biomedical optics express*, vol. 8, no. 8, pp. 3842–3855, 2017.
- [30] A. Appriou, A. Cichocki, and F. Lotte, “Towards robust neuroadaptive HCI,” in *Extended Abstracts of the 2018 CHI Conference on Human Factors in Computing Systems - CHI18*. ACM Press, 2018. [Online]. Available: <https://doi.org/10.1145/3170427.3188617>
- [31] S. B. Erdoğan, E. Özсарfati, B. Dilek, K. S. Kadak, L. Hanoğlu, and A. Akin, “Classification of motor imagery and execution signals with population-level feature sets: implications for

probe design in fNIRS based BCI,” *Journal of Neural Engineering*, vol. 16, no. 2, p. 026029, feb 2019. [Online]. Available: <https://doi.org/10.1088/1741-2552/aafdca>

- [32] S. Keshmiri, H. Sumioka, R. Yamazaki, and H. Ishiguro, “A non-parametric approach to the overall estimate of cognitive load using NIRS time series,” *Frontiers in Human Neuroscience*, vol. 11, feb 2017. [Online]. Available: <https://doi.org/10.3389/fnhum.2017.00015>
- [33] P. Sirpal, A. Kassab, P. Pouliot, and D. K. Nguyen, “fNIRS improves seizure detection in multimodal EEG-fNIRS recordings,” *Journal of Biomedical Optics*, vol. 24, no. 05, p. 1, feb 2019. [Online]. Available: <https://doi.org/10.1117/1.jbo.24.5.051408>
- [34] S. Bouktif, A. Fiaz, A. Ouni, and M. Serhani, “Single and multi-sequence deep learning models for short and medium term electric load forecasting,” *Energies*, vol. 12, no. 1, p. 149, 2019.
- [35] R. Kohavi *et al.*, “A study of cross-validation and bootstrap for accuracy estimation and model selection,” in *Ijcai*, vol. 14, no. 2. Montreal, Canada, 1995, pp. 1137–1145.

Appendix A. Performance results

Table A.1: Performance metrics for scenarios A and B: sensibility (SENS), specificity (SPEC), and general accuracy (ACC).

Classifier	Activity	Scenario A						Scenario B					
		Raw data		TFD-FB		HDM		Raw data		TFD-FB		HDM	
		SENS	PREC	SENS	PREC	SENS	PREC	SENS	PREC	SENS	PREC	SENS	PREC
SVM-L	Rest	0.538	0.589	0.611	0.664	0.669	0.627	0.469	0.401	0.469	0.336	0.466	0.518
	0-back	0.521	0.44	0.598	0.592	0.606	0.684	0.151	0.156	0.151	0.304	0.469	0.362
	2-back	0.399	0.345	0.628	0.478	0.787	0.734	0.182	0.199	0.182	0.134	0.483	0.38
	3-back	0.456	0.5	0.517	0.55	0.731	0.815	0.178	0.228	0.178	0.142	0.429	0.535
	ACC	0.498		0.596		0.687		0.287		0.287		0.462	
SVM-R	Rest	0.500	0.528	0.604	0.674	0.739	0.74	0.417	0.317	0.417	0.389	0.531	0.608
	0-back	0.483	0.47	0.617	0.599	0.656	0.715	0.227	0.302	0.227	0.515	0.491	0.513
	2-back	0.298	0.253	0.630	0.455	0.893	0.774	0.131	0.166	0.131	0.26	0.695	0.465
	3-back	0.347	0.371	0.476	0.5	0.818	0.865	0.154	0.144	0.154	0.06	0.512	0.481
	ACC	0.439		0.590		0.760		0.258		0.258		0.542	
RF-50	Rest	0.632	0.724	0.657	0.73	0.855	0.848	0.444	0.454	0.444	0.527	0.855	0.848
	0-back	0.652	0.568	0.593	0.567	0.858	0.874	0.234	0.229	0.234	0.223	0.857	0.873
	2-back	0.590	0.473	0.627	0.58	0.877	0.877	0.247	0.256	0.247	0.339	0.877	0.877
	3-back	0.654	0.647	0.706	0.576	0.889	0.889	0.226	0.206	0.226	0.175	0.889	0.889
	ACC	0.632		0.646		0.865		0.334		0.334		0.865	
RF-100	Rest	0.638	0.723	0.670	0.73	0.855	0.848	0.445	0.448	0.445	0.52	0.855	0.848
	0-back	0.649	0.585	0.638	0.575	0.858	0.874	0.234	0.232	0.234	0.231	0.858	0.874
	2-back	0.594	0.488	0.634	0.616	0.877	0.877	0.246	0.255	0.246	0.341	0.877	0.877
	3-back	0.651	0.626	0.717	0.643	0.889	0.889	0.221	0.209	0.221	0.18	0.889	0.889
	ACC	0.635		0.664		0.865		0.332		0.332		0.865	
CART-6	Rest	0.587	0.572	0.620	0.619	0.763	0.815	0.417	0.479	0.417	0.466	0.749	0.749
	0-back	0.443	0.341	0.491	0.472	0.808	0.745	0.207	0.179	0.207	0.259	0.837	0.678
	2-back	0.365	0.401	0.471	0.524	0.850	0.764	0.219	0.212	0.219	0.271	0.598	0.69
	3-back	0.430	0.537	0.467	0.42	0.807	0.829	0.261	0.199	0.261	0.271	0.770	0.805
	ACC	0.488		0.542		0.793		0.325		0.325		0.732	
CART-10	Rest	0.663	0.679	0.646	0.598	0.821	0.842	0.427	0.457	0.427	0.521	0.836	0.76
	0-back	0.550	0.468	0.509	0.529	0.828	0.84	0.213	0.208	0.213	0.271	0.845	0.786
	2-back	0.541	0.51	0.474	0.596	0.889	0.832	0.225	0.214	0.225	0.373	0.683	0.869
	3-back	0.482	0.577	0.428	0.358	0.839	0.829	0.235	0.206	0.235	0.198	0.885	0.889
	ACC	0.589		0.548		0.838		0.323		0.323		0.806	
LDA	Rest	0.583	0.574	0.709	0.556	0.629	0.381	0.410	0.652	0.410	0.534	0.613	0.401
	0-back	0.540	0.477	0.609	0.564	0.416	0.568	0.215	0.131	0.215	0.207	0.566	0.657
	2-back	0.327	0.316	0.386	0.477	0.380	0.455	0.249	0.133	0.249	0.162	0.554	0.533
	3-back	0.347	0.433	0.375	0.542	0.375	0.548	0.257	0.084	0.257	0.129	0.422	0.804
	ACC	0.483		0.540		0.457		0.362		0.362		0.537	

Appendix B. Confusion matrices for simulations

Table B.2: Confusion matrix for simulated scenario A (six frontal-cortex channels)

Classifier	Actual activity	Raw data				BFF				HDM			
		Predicted activity				Predicted activity				Predicted activity			
		Rest	0-back	2-back	3-back	Rest	0-back	2-back	3-back	Rest	0-back	2-back	3-back
SVM-L	Rest	4336	976	1184	863	4889	868	698	904	4612	1395	636	716
	0-back	1533	1381	159	68	1120	1859	123	39	991	2150	0	0
	2-back	1311	285	1105	499	1062	317	1531	290	847	0	2348	5
	3-back	873	8	319	1200	933	63	84	1320	444	0	0	1956
SVM-R	Rest	3888	1178	1164	1129	4961	778	643	977	5442	1176	296	445
	0-back	1292	1476	309	64	1089	1882	122	48	895	2246	0	0
	2-back	1591	317	808	484	1118	328	1456	298	707	0	2476	17
	3-back	1000	82	428	890	1046	63	90	1201	323	0	0	2077
RF-50	Rest	5327	764	682	586	5375	819	686	479	6243	456	393	267
	0-back	1069	1783	270	19	1027	1781	326	7	397	2744	0	0
	2-back	1285	185	1513	217	987	269	1855	89	393	0	2807	0
	3-back	747	2	98	1553	790	134	93	1383	267	0	0	2133
RF-100	Rest	5317	778	679	585	5370	733	698	558	6243	456	393	267
	0-back	988	1838	291	24	982	1806	353	0	397	2744	0	0
	2-back	1245	200	1560	195	973	206	1970	51	393	0	2807	0
	3-back	785	14	98	1503	687	86	85	1542	267	0	0	2133
CART-6	Rest	4210	1056	1349	744	4556	1183	1007	613	5997	548	432	382
	0-back	1353	1072	548	168	1008	1484	518	131	802	2339	0	0
	2-back	907	213	1283	797	955	159	1678	408	652	9	2446	93
	3-back	700	78	333	1289	834	195	363	1008	410	0	0	1990
CART-10	Rest	4998	942	707	712	4398	1165	1175	621	6197	548	332	282
	0-back	1017	1470	418	236	845	1663	495	138	496	2639	0	6
	2-back	836	191	1632	541	745	159	1907	389	444	0	2663	93
	3-back	689	69	258	1384	817	282	443	858	410	0	0	1990
LDA	Rest	4222	777	1130	1230	4090	650	1264	1355	2804	1660	1494	1401
	0-back	1095	1499	459	88	507	1770	618	246	729	1785	513	114
	2-back	1205	350	1010	635	715	394	1526	565	745	319	1456	680
	3-back	721	149	492	1038	456	94	549	1301	182	532	370	1316

Table B.3: Confusion matrix for simulated scenario B (single frontal-cortex channel)

Classifier	Actual activity	Raw data				BFF				HDM			
		Predicted activity				Predicted activity				Predicted activity			
		Rest	0-back	2-back	3-back	Rest	0-back	2-back	3-back	Rest	0-back	2-back	3-back
SVM-L	Rest	2953	1529	1558	1319	2473	2457	1572	857	3809	1044	1094	1412
	0-back	1438	489	870	344	1249	954	874	64	1902	1137	102	0
	2-back	1146	549	638	867	1458	891	428	423	1451	239	1216	294
	3-back	759	662	431	548	732	794	533	341	1009	5	103	1283
SVM-R	Rest	2335	1846	2153	1025	2864	2415	1037	1043	4474	1373	653	859
	0-back	1036	949	845	311	913	1619	557	52	1429	1612	0	100
	2-back	1315	791	532	562	1360	716	831	293	1369	200	1489	142
	3-back	908	603	544	345	861	933	461	145	1148	97	0	1155
RF-50	Rest	3339	1451	1566	1003	3877	1297	1333	852	6240	459	393	267
	0-back	1570	720	568	283	1562	702	705	172	397	2743	1	0
	2-back	1470	502	819	409	1498	310	1084	308	393	0	2807	0
	3-back	1147	399	359	495	1062	543	376	419	267	0	0	2133
RF-100	Rest	3297	1458	1551	1053	3825	1323	1296	915	6243	456	393	267
	0-back	1540	728	587	286	1558	727	697	159	397	2744	0	0
	2-back	1445	509	816	430	1466	329	1091	314	393	0	2807	0
	3-back	1128	413	358	501	1035	556	376	433	267	0	0	2133
CART-6	Rest	3522	1449	1500	888	3430	1491	1232	1206	5509	415	1036	399
	0-back	1892	563	568	118	1594	815	640	92	626	2130	385	0
	2-back	1731	448	678	343	1818	361	868	153	815	0	2207	178
	3-back	1310	266	347	477	751	786	213	650	404	0	63	1933
CART-10	Rest	3366	1471	1469	1053	3836	1384	1222	917	5595	454	1043	267
	0-back	1742	652	549	198	1448	852	754	87	486	2470	185	0
	2-back	1595	559	685	361	1419	355	1192	234	408	0	2782	10
	3-back	1186	372	348	494	1036	584	306	474	204	0	63	2133
LDA	Rest	4795	1089	1018	457	3932	1759	1185	483	2948	1388	1217	1806
	0-back	2655	411	67	8	2269	649	216	7	494	2063	156	428
	2-back	2516	137	427	120	2103	246	518	333	959	130	1704	407
	3-back	1722	273	203	202	1247	446	398	309	408	62	0	1930